



Pergamon

Acta mater. 49 (2001) 2341–2353



www.elsevier.com/locate/actamat

A THREE-DIMENSIONAL PHASE-FIELD MODEL FOR COMPUTER SIMULATION OF LAMELLAR STRUCTURE FORMATION IN γ TiAl INTERMETALLIC ALLOYS

Y. H. WEN^{1, 2†}, L. Q. CHEN², P. M. HAZZLEDINE^{3‡} and Y. WANG¹

¹Department of Materials Science and Engineering, The Ohio State University, Columbus, OH 43210, USA, ²Department of Materials Science and Engineering, The Pennsylvania State University, University Park, PA 16802 USA and ³Air Force Research Laboratory, Materials and Manufacturing Directorate, AFRL/MLLM, Wright-Patterson AFB, OH, 45433 USA

(Received 28 July 2000; received in revised form 18 December 2000; accepted 18 December 2000)

Abstract—A three dimensional phase-field model of $\alpha_2' \rightarrow \alpha_2 + \gamma$ transformation is developed to simulate the formation of coherent multi-domain lamellar structures in γ TiAl intermetallic alloys. The model takes into account the effect of coherency strain associated with the lattice rearrangement accompanying the phase transformation, and the anisotropy in interfacial energy. Simulation studies based on the model successfully predicted the essential features associated with the multi-domain lamellar structures observed experimentally. It is shown that the coherency strain accommodation is the dominating factor responsible for the formation of the lamellar structure. The neighboring lamellae of γ phase are found to have either a twin or a pseudo-twin relationship, with the former being dominant. It is found that strain-induced correlated nucleation plays an important role in the formation of the twined lamellae. The lamellar thickness is determined by the interplay among the elastic strain energy, interfacial energy and bulk chemical free energy. Domains within individual lamellae are isotropic and domain boundaries are smoothly curved. No special self-accommodating morphological patterns are observed on the $(0001)_{\alpha_2}$ plane, which is very different from the pattern formation predicted for the coherent hexagonal \rightarrow O-phase transformations. © 2001 Acta Materialia Inc. Published by Elsevier Science Ltd. All rights reserved.

Keywords: Lamellar structure; Computer Simulation; Alloys; Intermetallic; Phase transformations

1. INTRODUCTION

γ TiAl intermetallic alloys are the leading candidates for a new generation of high-temperature structural materials for applications in aerospace and automobile industries because of their high specific mechanical strength and good resistance to environmental attack at high temperatures [1–4]. However, the relatively poor ductility and fracture toughness of the single-phase γ TiAl alloys have been the main obstacles for their practical applications. Recent interest has been focusing on Ti-rich two-phase α_2 (Ti₃Al)+ γ (TiAl) alloys that contain a small amount of α_2 phase, forming a typical self-accommodating lamellar structure [5]. Typically the lamellar structure consists of twin- or pseudo-twin-related γ (L1₀) orientation variants and α_2 (DO₁₉) phase with the orientation relationship of $\{111\}_{\gamma}/\{(0001)_{\alpha_2}$ and

$\langle 1\bar{1}0 \rangle_{\gamma} // \langle 11\bar{2}0 \rangle_{\alpha_2}$ [6]. Such a multi-phase and multi-domain lamellar structure is what gives the alloys their outstanding combined properties of high-temperature strength and room-temperature ductility [7], but the processing routes and heat treatment are still largely empirical and, as a result, a particular lamellar structure cannot be produced in a controlled fashion. The main objective of this paper is to develop a computer model of phase transformation and microstructural evolution in two-phase γ + α_2 alloys which could allow detailed studies of lamellar thickness, domain size, and statistical distribution of lamellar and domain dimensions (all of which are known to have a direct effect on the mechanical properties [8, 9]) as functions of materials and processing parameters.

Even though recent advances in the theory of coherent transformations and corresponding computer modeling (see, e.g. Refs. [10–12]) have successfully predicted some of the interesting collective morphological patterns and kinetic phenomena, most studies deal with simple crystal lattice rearrangement such as cubic \rightarrow cubic or cubic \rightarrow tetragonal transformations.

† To whom all correspondence should be addressed. Tel.: +1-614-688-5616; fax: +1-614-292-1537.

E-mail address: Wen@bently.eng.ohio-state.edu (Y. H. Wen)

‡ UES, Inc., Dayton, OH 45432, USA.

Most of the simulations, to date, have been conducted in two-dimensions (2D). There is a large class of technologically important materials where phase transformations are far more complex and the basic microstructural features cannot be simulated in 2D. The Ti–Al system is a typical example, where the multi-domain lamellar structure is produced by multi-mode (diffusional and displacive) transformations where a high temperature disordered hexagonal (A3) phase decomposes into two ordered phases: DO₁₉ (hexagonal) and L1₀ (face-centered tetragonal). To the best of our knowledge, no computational model is available to describe the microstructural development in this system.

In this paper, we develop a 3D phase-field model for the formation and dynamic evolution of lamellar structures in two-phase γ TiAl alloys. In dealing with the multi-mode transformation dominated by elastic interactions taking place in the system, the phase-field method offers several advantages over the others (see Refs. [12, 13] for recent reviews). For example, the two physically distinctive transformation modes, i.e. the diffusional and displacive atomic rearrangement modes, can be effectively described with two types of field variables: a concentration field which describes the composition inhomogeneity and structural order parameter fields which characterize crystal symmetry changes. Their mutual interaction (nonlinear coupling) can be described by a non-equilibrium free energy formulated as a function of these fields. The long-range elastic interactions arising from the lattice misfit between the low-symmetry phase γ (L1₀) and the high-symmetry phase α_2 (DO₁₉), as well as among the various orientation variants of the γ phase can be taken into account conveniently by incorporating the elastic strain energy, formulated also as a function of the field variables, into the total free energy. The formation and dynamic evolution of arbitrary multi-domain morphologies during nucleation, growth and coarsening can be described with a single, consistent methodology with most of the input parameters based on the available experimental data.

In the following sections, we will first summarize the major experimental observations on the phase transformation path and crystallography of the transformation, upon which the stress-free transformation strain, elastic energy, chemical free energy and kinetic equations are formulated. Computer simulation techniques are introduced in Section 2 and simulation results are discussed in Section 3. Major results are summarized in Section 4.

2. PHASE TRANSFORMATION PATH IN γ TiAl AND ITS DESCRIPTION BY A PHASE-FIELD MODEL

2.1. Phase transformation path leading to the lamellar structure

Extensive experimental efforts have been made in the past decades (see Ref. [14] and references therein)

to characterize the crystallography of the phase transformation and microstructural development in γ TiAl-based intermetallic alloys. The parent phase α has a disordered *hcp* structure. One of the equilibrium product phases, α_2 , has an ordered *hcp* (DO₁₉) structure, while the other product phase, γ , has an ordered *fcc* (L1₀) structure. It has been well established that the lamellar structure does not occur through eutectoid reaction but results from the precipitation of γ lamellar in either a disordered α or a congruently ordered α_2' matrix, following one of the following two transformation paths: (1) $\alpha \rightarrow \alpha_2' \rightarrow \alpha_2 + \gamma$ (α_2' and α_2 have the same crystal structure but different composition) or (2) $\alpha \rightarrow \alpha_2 + \gamma$ [14]. The exact transformation path depends on the composition and heat treatment of the alloy. In view of the fact that the microstructures developed following the above two paths are very similar, one can simply focus on one reaction. This is because the $\alpha \rightarrow \alpha_2'$ congruent ordering does not alter the major characteristics of the microstructure [14]. In this paper we focus on the decomposition process of $\alpha_2' \rightarrow \alpha_2 + \gamma$. The possible effect of anti-phase domains and anti-phase domain boundaries in the congruently ordered α_2' phase on the precipitation of γ lamellae will be investigated in a separate paper.

2.2. Crystallography of phase transformation in γ TiAl and the stress-free transformation strain (SFTS)

According to the experimental observations [14], the formation of the lamellar structures involves simultaneously the following processes: (1) a crystal structure rearrangement from *hcp* type to *fcc* type; (2) a chemical composition change; and (3) ordering reactions from A3 to DO₁₉ in the *hcp* lattice and from A1 to L1₀ in the *fcc* lattice. The *hcp* \rightarrow *fcc* structure change can be accomplished simply by a combination of $\langle 11\bar{2} \rangle$ (111)_{fcc} shuffling along (111)_{fcc} planes, producing a homogeneous isotropic strain in the (111)_{fcc} planes and a change in d-spacing along [111]_{fcc} directions, like the martensitic transformation in Co [10]. For the $\alpha_2' \rightarrow \alpha_2 + \gamma$ transformation in γ TiAl, however, such a homogeneous shuffling is impossible because of the lack of three-fold symmetry of the L1₀ phase as compared to the *fcc* phase. According to the orders of the parent point group and the intersection group of the parent and product phases, and the orientation relationships mentioned above, the $\alpha_2' \rightarrow \alpha_2 + \gamma$ transformation results in six orientation variants of the γ phase, which has been confirmed by experimental observations (see, e.g. Ref. [7] and references therein). The six variants form three twin-related pairs and can be described by shears along $\pm[1\bar{1}00]_{\alpha_2}$, $\pm[10\bar{1}0]_{\alpha_2}$, $\pm[01\bar{1}0]_{\alpha_2}$ on (0001) _{α_2} . Following Grinfeld *et al.* [15], these three pairs of variants are labeled as (γ^0 , γ^{180}), (γ^{120} , γ^{300}), and (γ^{240} , γ^{60}), according to their anti-clockwise rotation with respect to variant γ^0 .

For convenience we formulate the SFTS in two steps: (a) shears along $\langle 10\bar{1}0 \rangle_{\alpha_2}$ which accomplish the stacking sequence change associated with the

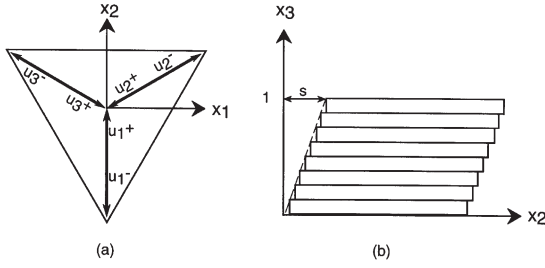


Fig. 1. (a) Schematic illustration of the six shear modes; (b) Displacement associated with u_1^+ , other displacements can be obtained by simple coordinate transformations.

$hcp \rightarrow fcc$ transition, leading to γ phase; (b) lattice distortion in the $(111)_{fcc}$ planes and a change in d-spacing along $[111]_{fcc}$ direction associated with the $L1_0$ ordering of the γ phase. If we take the α_2/α_2' phase as a reference state and set the x_1 , x_2 , and x_3 -axis parallel to the $[11\bar{2}0]_{\alpha_2}$, $[\bar{1}100]_{\alpha_2}$, and $[0001]_{\alpha_2}$, respectively, the displacements produced by the shears are (the six shear modes are schematically illustrated in Fig. 1(a) and the shear process associated with u_1^+ is shown in Fig. 1(b)):

$$\begin{aligned} u_1^+ &= 0, s x_3, 0 & u_1^- &= 0, -s x_3, 0 \\ u_2^+ &= -\sqrt{3}s x_3/2, -s x_3/2, 0 & u_2^- &= \sqrt{3}s x_3/2, s x_3/2, 0 \\ u_3^+ &= \sqrt{3}s x_3/2, -s x_3/2, 0 & u_3^- &= -\sqrt{3}s x_3/2, s x_3/2, 0 \end{aligned}$$

where s is the shear magnitude which is approximately equal to $1/(2\sqrt{2})$. The SFTS tensor u corresponding to the above displacements can be obtained via [16]

$$u_{ik} = \frac{1}{2} \left(\frac{\partial u_i}{\partial x_k} + \frac{\partial u_k}{\partial x_i} + \frac{\partial u_l}{\partial x_i} \frac{\partial u_l}{\partial x_k} \right),$$

which yields

$$\begin{aligned} u^+(1) &= \begin{pmatrix} 0 & 0 & 0 \\ 0 & 0 & s/2 \\ 0 & s/2 & s^2/2 \end{pmatrix}, \\ u^-(1) &= \begin{pmatrix} 0 & 0 & 0 \\ 0 & 0 & -s/2 \\ 0 & -s/2 & s^2/2 \end{pmatrix}; \\ u^+(2) &= \begin{pmatrix} 0 & 0 & -\sqrt{3}s/4 \\ 0 & 0 & -s/4 \\ -\sqrt{3}s/4 & -s/4 & s^2/2 \end{pmatrix}, \\ u^-(2) &= \begin{pmatrix} 0 & 0 & \sqrt{3}s/4 \\ 0 & 0 & s/4 \\ \sqrt{3}s/4 & s/4 & s^2/2 \end{pmatrix}; \end{aligned} \quad (1)$$

$$\begin{aligned} u^+(3) &= \begin{pmatrix} 0 & 0 & \sqrt{3}s/4 \\ 0 & 0 & -s/4 \\ \sqrt{3}s/4 & -s/4 & s^2/2 \end{pmatrix}, \\ u^-(3) &= \begin{pmatrix} 0 & 0 & -\sqrt{3}s/4 \\ 0 & 0 & s/4 \\ -\sqrt{3}s/4 & s/4 & s^2/2 \end{pmatrix}. \end{aligned}$$

The misfit strain associated with the tetragonality of γ TiAl can be described by the following

$$\begin{aligned} \epsilon_1 &= \begin{pmatrix} -\epsilon' & 0 & 0 \\ 0 & 2\epsilon/3 - \epsilon' & 0 \\ 0 & 0 & 0 \end{pmatrix}, \\ \epsilon_2 &= \begin{pmatrix} \epsilon/2 - \epsilon' & \sqrt{3}\epsilon/6 & 0 \\ \sqrt{3}\epsilon/6 & \epsilon/6 - \epsilon' & 0 \\ 0 & 0 & 0 \end{pmatrix}, \\ \epsilon_3 &= \begin{pmatrix} \epsilon/2 - \epsilon' & -\sqrt{3}\epsilon/6 & 0 \\ -\sqrt{3}\epsilon/6 & \epsilon/6 - \epsilon' & 0 \\ 0 & 0 & 0 \end{pmatrix} \end{aligned} \quad (2)$$

where ϵ_1 , ϵ_2 and ϵ_3 are associated with the three pairs of twin-related variants respectively. $\epsilon = (c/a_\gamma - 1)$ and $\epsilon' = (a_{\alpha_2} - \sqrt{2}a_\gamma)/a_{\alpha_2}$ is the largest mismatch between α_2 and γ [15]. It should be pointed out that the above misfit strain are exactly the same as those formulated by Grinfeld *et al.* [15]. The only difference is that they have chosen γ^0 as the reference system but in our case the reference system is the α_2 phase. Our choice is more convenient for the description of the phase transformation $\alpha_2' \rightarrow \alpha_2 + \gamma$. The elastic strain associated with the mismatch between the d-spacing between adjacent $(111)_\gamma$ and $(0001)_{\alpha_2}$ close-packed planes is $v \approx 2\sqrt{2}s(1 - \epsilon' + \epsilon/3) - 1$. Taking all these into consideration, the corresponding SFTS for the six variants can be expressed as

$$\begin{aligned} \epsilon^\circ(1) &= \begin{pmatrix} -\epsilon' & 0 & 0 \\ 0 & 2\epsilon/3 - \epsilon' & s/2 \\ 0 & s/2 & s^2/2 + v \end{pmatrix}, \\ \epsilon^\circ(2) &= \begin{pmatrix} -\epsilon' & 0 & 0 \\ 0 & 2\epsilon/3 - \epsilon' & -s/2 \\ 0 & -s/2 & s^2/2 + v \end{pmatrix}; \end{aligned}$$

$$\begin{aligned} \epsilon^\circ(3) &= \begin{pmatrix} \epsilon/2 - \epsilon' & \sqrt{3}\epsilon/6 & -\sqrt{3}s/4 \\ \sqrt{3}\epsilon/6 & \epsilon/6 - \epsilon' & -s/4 \\ -\sqrt{3}s/4 & -s/4 & s^2/2 + \nu \end{pmatrix}, & (3) \\ \epsilon^\circ(4) &= \begin{pmatrix} \epsilon/2 - \epsilon' & \sqrt{3}\epsilon/6 & \sqrt{3}s/4 \\ \sqrt{3}\epsilon/6 & \epsilon/6 - \epsilon' & s/4 \\ \sqrt{3}s/4 & s/4 & s^2/2 + \nu \end{pmatrix}; \\ \epsilon^\circ(5) &= \begin{pmatrix} \epsilon/2 - \epsilon' & -\sqrt{3}\epsilon/6 & \sqrt{3}s/4 \\ -\sqrt{3}\epsilon/6 & \epsilon/6 - \epsilon' & -s/4 \\ \sqrt{3}s/4 & -s/4 & s^2/2 + \nu \end{pmatrix}, \\ \epsilon^\circ(6) &= \begin{pmatrix} \epsilon/2 - \epsilon' & -\sqrt{3}\epsilon/6 & -\sqrt{3}s/4 \\ -\sqrt{3}\epsilon/6 & \epsilon/6 - \epsilon' & s/4 \\ -\sqrt{3}s/4 & s/4 & s^2/2 + \nu \end{pmatrix} \end{aligned}$$

The above six variants correspond to γ^0 , γ^{180} , γ^{120} , γ^{300} , γ^{240} , γ^{60} , respectively. They can be divided into three pairs, (1, 2), (3, 4), and (5, 6), two variants in each pair will form twin when they come into contact along $[0001]_{\alpha_2}$ while two variants from different pairs will form pseudo-twin.

2.3. Mathematic description of the $\alpha_2' \rightarrow \alpha_2 + \gamma$ phase transformation by a phase-field model

In the phase-field method, an arbitrary multi-phase and multi-domain microstructure with compositional and structural heterogeneities is characterized by a set of continuum field variables. As has been discussed earlier, the precipitation of γ from α_2' produces six orientation variants of the γ phase. In the phase-field approach, the spatial distribution of the six orientation variants can be described by introducing six structural order parameter fields.

$$\eta_1(\mathbf{r}, t), \eta_2(\mathbf{r}, t), \dots, \eta_6(\mathbf{r}, t)$$

where t is time and \mathbf{r} is the spatial coordinate vector. Each of these six structural order parameter fields assumes a non-zero value, say $\pm\eta_0$, within a particular domain and vanishes within the α_2/α_2' phase and other domains. The $\eta \rightarrow -\eta$ transition describes rigid-body translation leading to anti-phase domains. The composition variation among the coexisting phases can be characterized by a concentration field, $c(\mathbf{r}, t)$. We note that the anti-phase domains within the α_2'/α_2 phase are ignored in this formulation for simplicity.

The spatio-temporal evolution of these field variables completely defines the evolution of an arbitrary microstructure, including the shape, size, and spatial distribution of all the constituent phase/orientation variants and anti-phase domains. The temporal evolution of the structural order parameters can be

obtained by solving the time-dependent Ginzburg–Landau equation

$$\frac{\partial \eta_p(\mathbf{r}, t)}{\partial t} = -L \frac{\delta F}{\delta \eta_p(\mathbf{r}, t)} + \xi_p(\mathbf{r}, t); \quad p = 1, 2, \dots, 6. \quad (4)$$

while the temporal evolution of the concentration field can be described by the non-linear Cahn–Hilliard diffusion equation

$$\frac{\partial c(\mathbf{r}, t)}{\partial t} = M \nabla^2 \frac{\delta F}{\delta c(\mathbf{r}, t)} + \zeta(\mathbf{r}, t); \quad (5)$$

where L and M are kinetic coefficients characterizing structural relaxation and diffusional mobility; F the total free energy of the system under consideration, $\xi_p(\mathbf{r}, t)$ and $\zeta(\mathbf{r}, t)$ are Langvin random noise terms which are related to thermal fluctuations in the structural order parameter and composition, respectively. They are assumed to be Gaussian distributed and their correlation properties meet the requirements of the fluctuation-dissipation theorem [17]. The Langvin noise terms allow homogeneous nucleation leading a system from a metastable state to a stable state. In this study, only homogeneous nucleation is considered. Heterogeneous nucleation of γ phase on stacking faults will be considered in a separate paper.

2.4. Thermodynamic description of the phase transformation: formulation of chemical free energy and elastic strain energy

The total free energy, F , in equations (4) and (5) defines the thermodynamic features of the phase transformation. In the phase-field approach, the total free energy is formulated as a functional of the field variables. For a coherent phase transformation [10], the total free energy should consist of two terms: the chemical free energy (F_{ch}) and the elastic strain energy (E_{el}), i.e. $F = F_{ch} + E_{el}$.

The non-equilibrium chemical free energy as a function of the field variables can be approximated by the Ginzburg–Landau coarse-grained free energy functional, which contains a local specific free energy, $f(c, \eta_1, \eta_2, \dots, \eta_6)$, and gradient energy terms, e.g.

$$\begin{aligned} F_{ch} = \int_V \left[\frac{1}{2} \rho (\nabla c)^2 + \frac{1}{2} \sum_{i,j,p} \lambda_{ij}^{(p)} \left(\frac{\partial \eta_p}{\partial r_i} \right) \left(\frac{\partial \eta_p}{\partial r_j} \right) \right. \\ \left. + f(c, \eta_1, \eta_2, \dots, \eta_6) \right] dV \end{aligned} \quad (6)$$

where ρ and $\lambda_{ij}^{(p)}$ are gradient energy coefficients. The integration in equation (6) is carried out over the entire system volume V . As usual, the gradient terms in equation (6) provide an energy penalty to inhomogeneities in composition and structural order parameter fields which take place mainly at interfaces.

The local specific free energy $f(c, \eta_1, \eta_2, \dots, \eta_6)$ in equation (6) defines the basic thermodynamic properties of the system. It can be approximated either by a Bragg-William type of mean-field model or by a Landau type polynomial expansion. In this paper, the latter is adopted and a simple polynomial is employed,

$$f(c, \eta_1, \eta_2, \dots, \eta_6) = \frac{A_1}{2}(c - c_1)^2 + \frac{A_2}{2}(c_2 - c) \sum_{p=1}^6 \eta_p^2 - \frac{A_3}{4} \sum_{p=1}^6 \eta_p^4 + \frac{A_4}{6} \left(\sum_{p=1}^6 \eta_p^2 \right)^3, \quad (7)$$

where c_1 and c_2 are constants close to the equilibrium compositions of the α_2 and γ phases, respectively. A_1 to A_4 are positive constants which should be chosen to fit the local specific free energy based on available experimental data. Minimization of the local specific free energy given in equation (7) with respect to both composition and structural order parameters yields a two-phase equilibrium with six orientation variants of the γ phase because the free energy functional has six degenerated minima corresponding to the six orientation variants.

According to the elasticity theory of multi-phase coherent solids developed by Khachaturyan [10], in the homogeneous modulus approximation, the elastic strain energy E_{el} generated by an arbitrary concentration or structure heterogeneity can be presented as a close-form functional of concentration and structural order parameter fields. In the case where the strain is predominantly caused by the structural order parameter field heterogeneity, the stress-free strain can be expanded with respect to the structural order parameter. As the $\eta \rightarrow -\eta$ transition does not change the macroscopic stress-free strain, the first non-vanishing term of the expansion is of second order in $\eta_p(\mathbf{r})$, i.e. $\epsilon_{ij}^\circ(\mathbf{r}) = \sum_{p=1}^6 \eta_p^2(\mathbf{r}) \epsilon_{ij}^\circ(p)$, where the tensor $\epsilon^\circ(p)$ is the SFTS tensor of orientation variant p of the γ phase when the corresponding order parameter assumes its equilibrium value, i.e. $\eta_p^2(\mathbf{r}) = 1$. Following our previous work (see [18–20] and references therein), the elastic strain energy can be expressed as

$$E_{el} = \frac{V}{2} C_{ijkl} \bar{\epsilon}_{ij} \bar{\epsilon}_{kl} - V C_{ijkl} \bar{\epsilon}_{ij} \sum_{p=1}^6 \epsilon_{kl}^\circ(p) \overline{\eta_p^2(\mathbf{r})} + \frac{V}{2} C_{ijkl} \sum_{p=1}^6 \sum_{q=1}^6 \epsilon_{ij}^\circ(p) \epsilon_{kl}^\circ(q) \overline{\eta_p^2(\mathbf{r}) \eta_q^2(\mathbf{r})} - \frac{1}{2} \sum_{p=1}^6 \sum_{q=1}^6 \oint \frac{d^3 \mathbf{g}}{(2\pi)^3} B_{pq}(\mathbf{n}) \{ \eta_p^2(\mathbf{r}) \}_\mathbf{g}^* \{ \eta_q^2(\mathbf{r}) \}_\mathbf{g} \quad (8)$$

where $\{ \dots \}$ represent the volume average of (\dots) ; V the total volume of the system; C_{ijkl} the elastic moduli tensor; and ϵ the elastic strain tensor. $B_{pq}(\mathbf{n})$ is a two-body interaction potential given by

$$B_{pq}(\mathbf{n}) = n_i \sigma_{ij}^\circ(p) \Omega_{jk}(\mathbf{n}) \sigma_{kl}^\circ(q) n_l \quad (9)$$

where $\mathbf{n} = \mathbf{g}/g$ is a unit vector in reciprocal space and n_i is its i th component, $\sigma_{ij}^\circ(p) = C_{ijkl} \epsilon_{kl}^\circ(p)$ and $\Omega_{ij}(\mathbf{n})$ is a Green function tensor which is inverse to the tensor

$$\Omega_{ij}^{-1}(\mathbf{n}) = C_{ijkl} n_k n_l, \quad \{ \eta_q^2(\mathbf{r}) \}_\mathbf{g} = \int \frac{d^3 \mathbf{g}}{(2\pi)^3} \eta_q^2(\mathbf{r}) \exp(-i\mathbf{g} \cdot \mathbf{r})$$

is the Fourier transform of $\eta_q^2(\mathbf{r})$ and $\{ \eta_p^2(\mathbf{r}) \}_\mathbf{g}^*$ is the complex conjugate of $\{ \eta_p^2(\mathbf{r}) \}_\mathbf{g}$

The first two terms on the right hand side of the above equation describe the elastic energy due to a homogeneous deformation. The third term describes the elastic energy associated with deforming the stress-free product phase back into its geometrical shape before the transformation and the last term describes the heterogeneous relaxation of the precipitates which does not produce any macroscopic shape change but affect the shape, size and spatial distribution of the product phase. Please note that the integration has to be carried out over the first Brillouin zone where a volume of $(2\pi)^3/V$ about $g = 0$ is excluded from the integration. In this work, the macroscopic homogeneous strain $\bar{\epsilon}_{ij}$ is assumed to be zero which corresponds to a system of a single grain embedded in a polycrystalline material. As a result, the first two terms vanish. It should be noted that incoherency is not considered in the elastic energy calculation.

2.5. The explicit forms of the kinetic equations and input parameters

Substituting the chemical free energy [equation (6)] and the strain energy [equation (8)] into the kinetic equations (4) and (5), the explicit form of the equations can be obtained:

$$\frac{\partial \eta_p(\mathbf{r}, t)}{\partial t} = -L \left(- \sum_{ij=1}^3 \lambda_{ij}^{(p)} \frac{\partial^2 \eta_p(\mathbf{r}, t)}{\partial r_i \partial r_j} + \frac{\partial f}{\partial \eta_p(\mathbf{r}, t)} + \frac{\delta E_{el}}{\delta \eta_p(\mathbf{r}, t)} \right) + \xi_p(\mathbf{r}, t) \\ \frac{\partial c(\mathbf{r}, t)}{\partial t} = M \nabla^2 \left(-\rho \nabla^2 c(\mathbf{r}, t) + \frac{\partial f}{\partial c(\mathbf{r}, t)} \right) + \zeta(\mathbf{r}, t). \quad (10)$$

For the convenience of numerical solution, the kinetic equations are transformed into dimensionless form through the introduction of a reduced time, defined as $\tau = L |\Delta f| t$, and reduced spatial coordinates, defined as $u_i = x_i/l$. In these definitions, $|\Delta f|$ is the chemical driving force for the phase transformation under consideration and l is the length unit of the computational grid size. Substituting these reduced variables into equations (6), (7) and (8), we get the dimensionless form of the kinetic equations:

$$\frac{\partial \eta_p(\mathbf{u}, \tau)}{\partial \tau} = - \left(- \sum_{ij=1}^3 \beta_{ij}^{(p)} \frac{\partial^2 \eta_p(\mathbf{u}, \tau)}{\partial u_i \partial u_j} + \frac{\partial f_a}{\partial \eta_p(\mathbf{u}, \tau)} + \phi \frac{\delta E_{el}'}{\delta \eta_p(\mathbf{u}, \tau)} \right) + \xi_p'(\mathbf{u}, \tau) \quad (11)$$

$$\frac{\partial c(\mathbf{u}, \tau)}{\partial \tau} = \vartheta \nabla^2 \left(-\alpha \nabla^2 c(\mathbf{u}, \tau) + \frac{\partial f_a}{\partial c(\mathbf{u}, \tau)} \right) + \zeta'(\mathbf{u}, \tau); \quad (12)$$

where

$$\beta_{ij}^{(p)} = \frac{\lambda_{ij}^{(p)}}{l^2|\Delta f|}; \quad \phi = \frac{1}{|\Delta f|}; \quad (13)$$

$$\vartheta = \frac{M}{Ll^2}; \quad \alpha = \frac{\rho}{|\Delta f|l^2}; \quad (14)$$

$$f_a = \frac{a_1}{2}(c-c_1)^2 + \frac{a_2}{2}(c_2-c)\sum_p \eta_p^2 - \frac{a_3}{4}\sum_p \eta_p^4 + \frac{a_4}{6}\left(\sum_p \eta_p^2\right)^3 \quad (15)$$

with

$$a_i = \frac{A_i}{|\Delta f|}, \quad i = 1,2,3,4.$$

and

$$\xi_p'(\mathbf{u}, \tau) = \frac{\xi_p(\mathbf{r}, t)}{L|\Delta f|}, \quad \zeta'(\mathbf{u}, \tau) = \frac{\zeta(\mathbf{r}, t)}{L|\Delta f|},$$

$$\frac{\delta E_{el}'}{\delta \eta_p(\mathbf{u}, \tau)} = 2\eta_p(\mathbf{u}, \tau)$$

$$\left(-C_{ijkl}\bar{\epsilon}_{ij}\epsilon_{kl}^\circ(p) + \sum_{q=1}^6 \langle C_{ijkl}\epsilon_{ij}^\circ(p)\epsilon_{kl}^\circ(q)\eta_q^2(\mathbf{u}, \tau) - \{B_{pq}(\mathbf{n})\{\eta_q^2(\mathbf{u}, \tau)\}_{\mathbf{g}'}\} \mathbf{u} \right)$$

where $\mathbf{g}' = \mathbf{gl}$.

To solve the above kinetic equations, we need to specify the following input material parameters

- dimensionless parameters $\beta_{ij}^{(p)}$, ϕ , ϑ , and α . $\beta_{ij}^{(p)}$ and α characterize the magnitudes of specific gradient energies with respect to the chemical driving force. ϕ is a normalization factor with respect to the depth of the local specific free energy potential well.
- all the constants in defining the local chemical free energy (c_1 , c_2 , a_1 , a_2 , a_3 , a_4 in equation (15));
- elastic moduli C_{ijkl} of the material for calculating the strain energy in equation (8);
- deformation parameters (ϵ , ϵ') for determining the SFTS tensor of the $\alpha_2' \rightarrow \gamma$ transition in equation (3).

and some numerical parameters including

- mesh dimensions (n_x , n_y , n_z) and its discretization in space (dx , dy , dz) and time (dt);
- boundary and initial conditions.

In this work, the gradient energy coefficients ($\beta_{ij}^{(p)}$ tensor) are assumed to be variant-independent and only diagonal terms are non-zero, i.e. $\beta_{ij}^{(p)} = \beta_{ij}\delta_{ij}$. Due to the fact that the parent phase (*hcp*) is transversely

isotropic on the close-packed plane ($x_1o x_2$ plane for the chosen reference system), we further assume that $\beta_{11}=\beta_{22}=5\beta_{33}=3.0$. A relatively smaller β_{33} is chosen because the x_3 direction is perpendicular to the close-packed plane, it is assumed that the specific interfacial energies inside the close-packed plane is about 5 to 10 times higher than those off the close-packed plane. ϕ is assumed to be 15. ϑ is assumed to be 1. α is assumed to be 3.0 which is the same as β_{11} . c_1 and c_2 are chosen to be 0.38 and 0.48, respectively, according to the phase diagram [4] and the mean composition of the alloy is assumed to be 0.46, which is very close to the single γ -phase region for the purpose to have a relatively higher volume fraction of the γ -phase. a_1 – a_4 are assumed to be 1149.43, 172.41, 57.47 and 43.1, respectively, to give a qualitatively correct description of the thermodynamics of the system (Fig. 2). The elastic moduli tensor of the system is assumed to be homogeneous and those for the parent α_2 phase at 290 K are employed to represent the elastic moduli of the system. All the Voigt elastic constants are zero except that: $C_{11} = C_{22} = 175$ GPa; $C_{33} = 220$ GPa; $C_{12} = 88.7$ GPa; $C_{13} = C_{23} = 62.3$ GPa; $C_{44} = C_{55} = 62.2$ GPa; $C_{66} = (C_{11} - C_{12})/2$, which were taken from experimental data [21]. Deformation parameters ($\epsilon = 0.02$, $\epsilon' = 0.03$) can be found in literature [15]. The simulation is carried out on a mesh with $n_x = n_y = 64$, $n_z = 128$ grid points. A larger dimension along x_3 direction is chosen because the lamellar structure is highly heterogeneous along this direction. $du_x = du_y = du_z = 0.5$ and $d\tau = 0.002$ are set for the calculation. Periodic boundary condition is imposed along the three axes.

3. RESULTS AND DISCUSSION

3.1. Formation of lamellar structures

The simulated 3D microstructural evolution is shown in Fig. 3, where we plot the values of $(\eta_1^2 -$

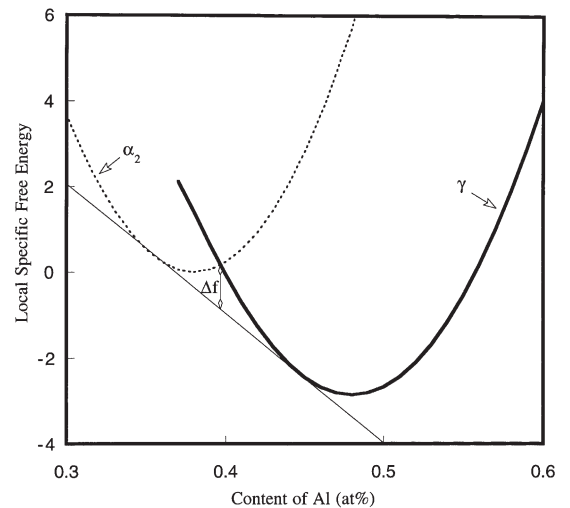


Fig. 2. Local specific free energy for parent and product phases as a function of the content of Al.

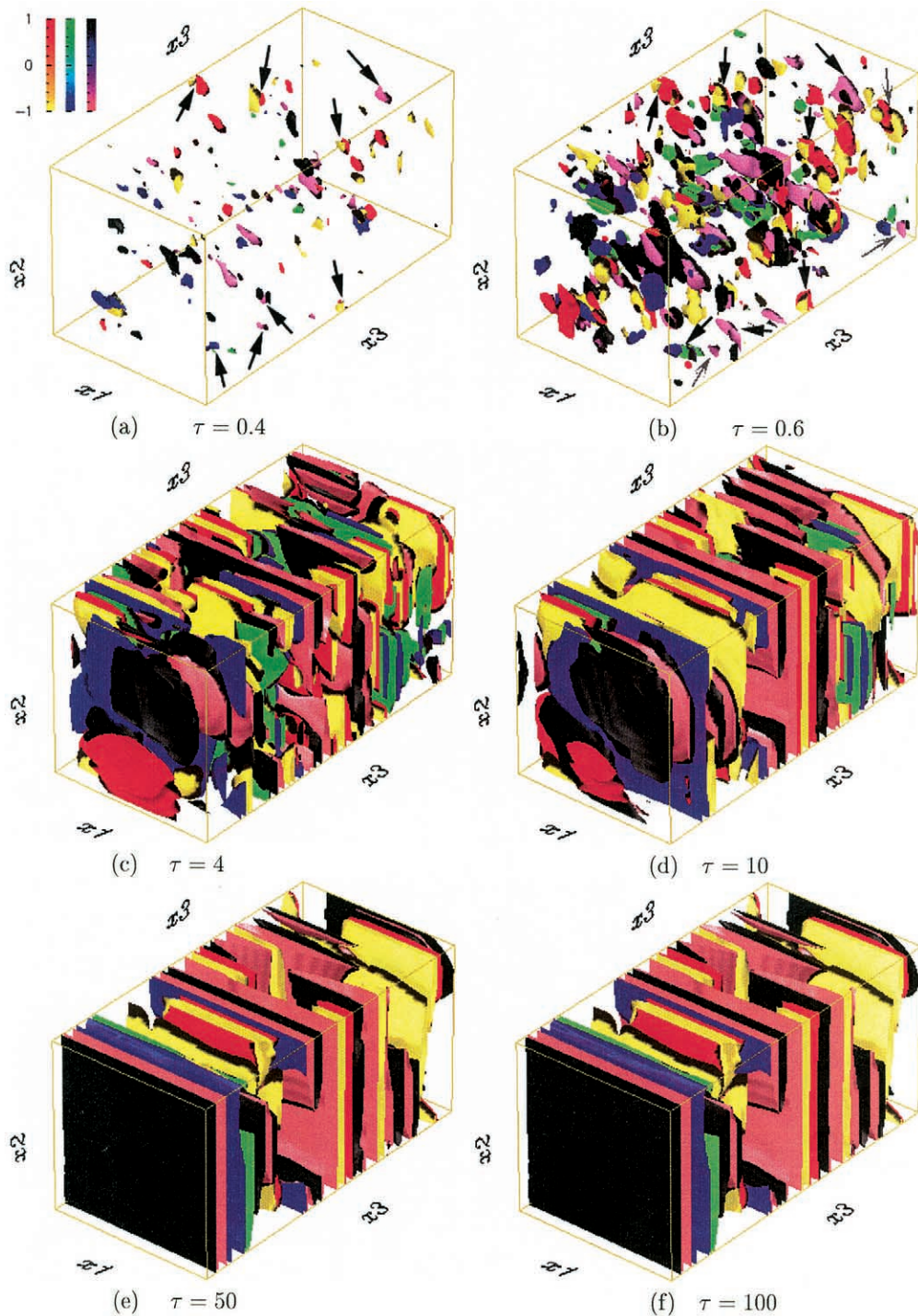


Fig. 3. Simulated morphological evolution in the whole unit cell. Colors red, yellow, green, purple, black, and pink denote variants 1 through 6.

η_2^2), $(\eta_3^2 - \eta_4^2)$ and $(\eta_5^2 - \eta_6^2)$, respectively, by isosurfaces with different colors. The positive and negative values of the isosurfaces represent variants (1, 3, 5) and (2, 4, 6), respectively. Three color bars each with two major colors are illustrated in the up-left corner of Fig. 3(a). In such a color scheme, variants 1–6 correspond to colors red, yellow, green, purple, black,

pink, respectively, and the three twin-related pairs (1, 2), (3, 4), and (5, 6) correspond to (red, yellow), (green, purple) and (black, pink), respectively.

The simulation is started from a homogeneous microstructure of supersaturated α_2' phase. The nucleation process was simulated by random fluctuations both in composition and structural order para-

mers. At $\tau = 0.4$ (Fig. 3(a)), one can find some randomly distributed nuclei of all six variants. It is at this stage that the random fluctuations are switched off and the system chooses its own dynamic path for further evolution. We find that a lot of variants appear in couples (e.g. refer to those areas in Fig. 3(a) indicated by arrows). A close examination reveals that most of them are twin-related, i.e. they belong to one of the variant combinations (1, 2), (3, 4), or (5, 6). This result indicates that self-accommodation starts to operate at the very nucleation stage of the γ variants. This is in agreement with previous works on strain-induced martensitic transformations [22]. After a short time aging to $\tau = 0.6$ (Fig. 3(b)), most of the variants are in thin plate morphology parallel to the $(0001)_{\alpha_2}$ plane. Comparing with Fig. 3(a), one can find that all the composite particles consisting of twin or pseudo-twin-related variants grow. In the meantime, some more twin-related variant pairs emerge, e.g. those areas indicated by gray arrows in Fig. 3(b), which have been nucleated in earlier stage but failed to show up in Fig. 3(a) because of their small values relative to that of the isosurfaces. With further aging up to $\tau = 4$, more lamellae of γ phase develop (Fig. 3(c)). At $\tau = 10$ (Fig. 3(d)), many lamellae extend across the entire unit cell. However, the microstructural evolution seems significantly slows down after this moment indicating the end of the growth stage and starting of the coarsening stage. The lamellar structure has the tendency to become more and more regular with coarsening (Fig. 3(d) and (e)). For example, after a relatively long-time coarsening up to $\tau = 50$, a black variant (variant 5) is spread over the whole external $x_1o x_2$ surface (Fig. 3(e)). But the volume fraction of the product phase changes little. This is obvious by following the microstructural evolution from $\tau = 50 \rightarrow 100$ (Fig. 3(e) and (f)). Although locally some plates become more regular through lateral growth on the $(0001)_{\alpha_2}$ plane, the overall volume fraction of the product phase and the microstructure looks quite the same. It should be pointed out that the volume fraction of the product phase is about 30% less than the equilibrium volume fraction predicted from the f - c curve presented in Fig. 2.

3.2. Microstructural evolution on a particular plane normal to the $(0001)_{\alpha_2}$

To examine in details some of the features accompanying the microstructural development, in Fig. 4 we show microstructural evolution on the external $x_2o x_3$ plane of Fig. 3, which is normal to the $(0001)_{\alpha_2}$ plane. The color scheme is roughly the same as that employed in the previous 3D presentation and the accurate color correspondence of the six variants is illustrated in Fig. 4(i). At $\tau = 0.4$, one can find all the six variants and the arrangement of these variants already show certain anisotropy. The noise terms are switched off at this time. Shortly after that, small thin plates emerge as shown in Fig. 4(b). This is followed by mainly lateral growth and coalescence of these

variants parallel to the $(0001)_{\alpha_2}$ plane (Fig. 4(c)). At $\tau = 10$ (Fig. 4(d)), several plates extend across the entire unit cell forming very regular lamellae parallel to the $(0001)_{\alpha_2}$ plane. For example, one can find several lamellae pile up regularly in the central area. A variant in brown (variant 5) in the central area is composed of two parts with $\pm\eta_5$, respectively, separated by two thin layers of the α_2 phase, indicated by two white arrows. In the lower left part of the same figure, one can find an alternating arrangement (indicated by a black arrow) consisting of two twin-related variants (3, 4) in green and blue, respectively. It is interesting to note the serrated morphology of the α_2/γ interface. Similar phenomenon was observed in the ϵ -Martensitic transformation [23], which involves a $fcc \rightarrow hcp$ transformation. The serrated morphology of the hcp/fcc interface was attributed to the shear nature of the structural transition and the alternation shear mode associated with various variants [24]. The present interface morphology can be explained in the same way although it is simpler because the shear direction is simply opposite for the two twin-related variants.

Due to the stochastic nature of the nucleation process, there is a thickness distribution of the lamellae, which provides the opportunity for coarsening. During the coarsening process, some variants grow while some others shrink. For example, the pink variant (variant 6) in the central area, which is indicated by a black arrow in Fig. 4(e), grows while the red variant (variant 1) below it shrinks. The continuous red lamella (see its shape in Fig. 4(d)) breaks up leading to a disk-like inclusion between the pink and yellow variants (variants 6 and 2, respectively) and eventually disappears. A close examination of the morphology of the disk-like inclusion indicates that its lower twin-related interface with variants 2 remains quite flat while in contrast the upper pseudo-twin-related interface is not, which implies that the pseudo-twin interface is probably easier to break up due to the relatively higher elastic energy as compared to the twin-related interfaces. With further coarsening, the inclusion finally disappears as shown in Fig. 4(f). At the top part of Fig. 4(e), there is a disk-like composite particle consisting of two twin-related variants as indicated by a black double-arrow. It is interesting to note that the α_2/γ interface is curved while the γ/γ interface is flat and parallel to the $(0001)_{\alpha_2}$ plane. When the composite particle come into contact with another brown variant at the very top during continued coarsening, two curved α_2/γ interfaces for the brown (above) and pink (low) are replaced by a flat γ/γ interface (Fig. 4(f)). The contacting brown and pink variants at the top are actually twin-related variants 5 and 6, respectively. Again, there is a serrated interface between the couple and the α_2 phase near the double arrow (Fig. 4(f)). The serrated morphology of the interface keeps unaltered during their further coarsening on the $(0001)_{\alpha_2}$ plane (refer to Fig. 4(f) and (g)). In the meantime, the brown variant below

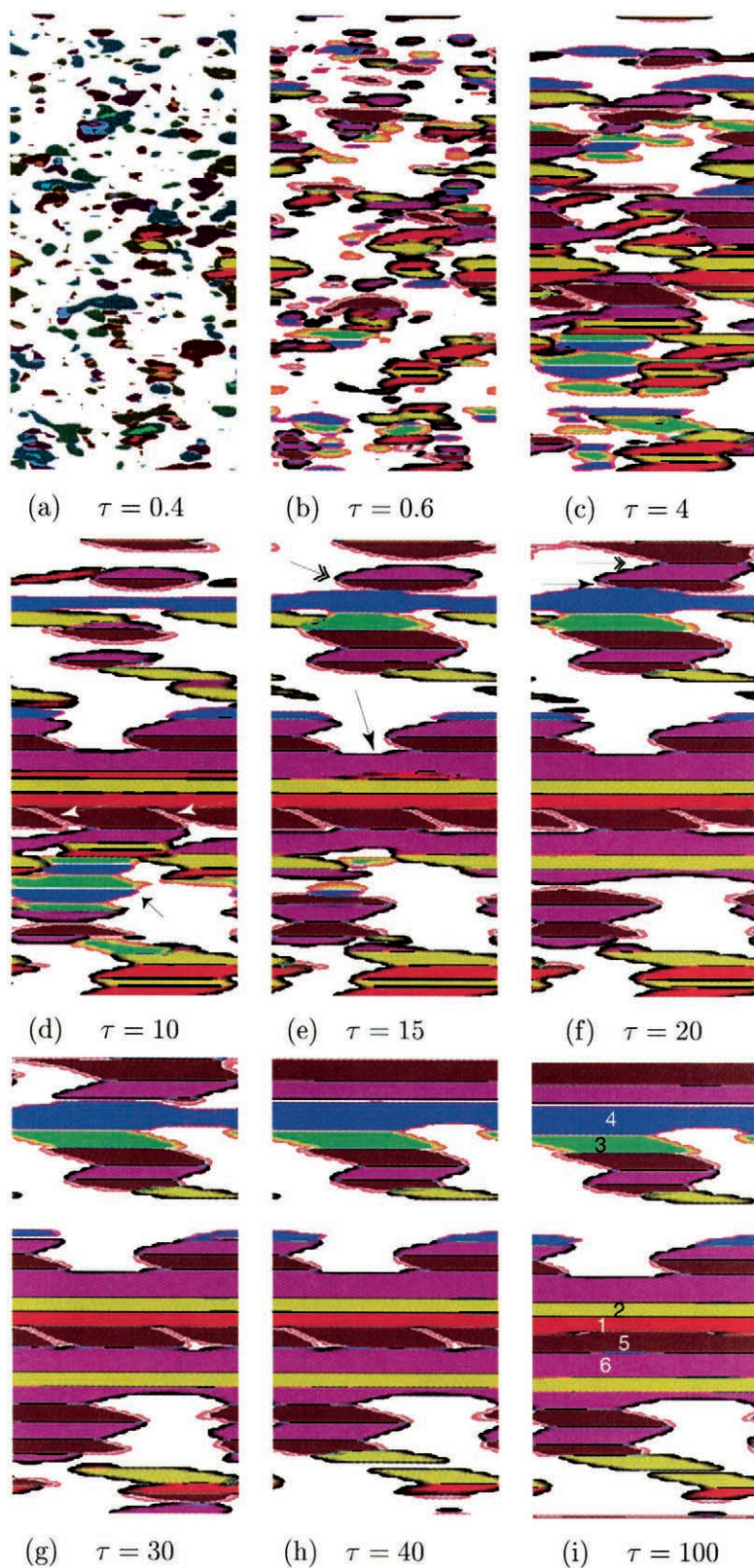


Fig. 4. Morphological evolution on the $x_2o x_3$ surface plane of the 3D unit cell. The color and variant number correspondence is shown in Fig. 4(i).

them (indicated by a black arrow in Fig. 4(f)) shrinks leaving a very thin layer of untransformed matrix between variant 6 (above) and variant 4 (below) as shown in Fig. 4(g), which is very stable against further coarsening. It still remains unchanged even after a very long-time coarsening up to $\tau = 100$ (Fig. 4(i)). This phenomenon has been observed by experiments [7]. It should be pointed out that the evolution process may be different if the pink and blue variants are twin-related. During this coarsening period from $\tau = 40 \rightarrow 100$, the two thin layers of α_2 phase within a γ lamella observed in Fig. 4(d) finally disappear while the rest of microstructure keeps almost unchanged indicating that the coarsening of microstructure at the later stage is relatively slow.

3.3. Mutual arrangement of the six orientation variants

To examine the twin vs. pseudo-twin relationships among the six γ variants, in Fig. 5 we show all couples of variants in contact at the final stage of the simulation on the same plane as in Fig. 4. For six variants, we could have up to 15 different combination of variants. Only three couples, namely (1, 2), (3, 4), and (5, 6) are twin-related while all the rest are pseudo-twin-related when they stack together normal to the $(0001)_{\alpha_2}$ plane. In Fig. 5, one can find all the three twin-related couples as shown in Fig. 5(a)–(c). However, only 4 out of the 12 possible pseudo-twin-related couples exist (Fig. 5(d)–(g)), and the total amount of pseudo-twin-related variants is smaller as compared to those twin-related. This may be attributed to the strain-induced correlated nucleation process discussed earlier. Also the formation of the twin-related couples can better accommodate the lattice misfit between them and therefore they are favored during growth and coarsening stages. It may worth noting that the fraction of the three twin-related couples is also very different. The amount of the couple in Fig. 5(c), i.e. variant 5 and 6, is significantly higher than two other couples as shown in Fig. 5(a) and (b). This difference is mainly due to the stochastic nature of the nucleation. The thickness of various lamellae vary significantly too which is in line with experimental observations [7].

3.4. Microstructural evolution on $(0001)_{\alpha_2}$ plane

In Fig. 6, we show morphological evolution on one $(0001)_{\alpha_2}$ plane, namely x_1ox_2 of the 3D unit cell shown in Fig. 3 with $x_3 = 50$. This plane is chosen for the purpose to gain more insight into how the in-lamella domain structure (including interface between two anti-phase domains as highlighted in Fig. 4(d) by the white arrows) evolves during the aging process. The shades of gray correspond to the relative value of $(\eta_1^2 - \eta_2^2) + (\eta_3^2 - \eta_4^2) + (\eta_5^2 - \eta_6^2)$. The higher the value, the brighter the shade. Therefore, the white, black, and gray areas represent, respectively, variants (1, 3, or 5), (2, 4, or 6), and α_2 phase. At the moment that the noise terms are turned off (Fig. 6(a)), all six variants coexist on the plane together with some α_2 phase. After a short aging to $\tau = 0.6$ (Fig. 6(b)), some variants grow and in the meantime variants 1 and 6 disappear. At $\tau = 2$ (Fig. 6(c)), variant 4 at the lower-left corner disappears and another one at the central area shrinks and eventually disappears at $\tau = 4$ (Fig. 6(d)) with further growth of variants 2, 3 and 5. After a relatively long-time aging up to $\tau = 10$ (Fig. 6(e)), the dominant variant left is variant 5 (white) at the expenses of disappearance of variant 3 and shrinkage of variant 2 (black). Further coarsening causes the disappearance of variant 2 resulting in several domains of variant 5 embedded in the α_2 phase (Fig. 6(f)). Variant 5 itself is separated into two domains on the plane (considering periodic boundary condition). The structural order parameters η_5 associated with them are respectively positive and negative as indicated in Fig. 6(f). The composition of the thin layers in-between the two domains of η_5 equals to that of the α_2 phase. Therefore, they are not anti-phase domain boundaries (APBs), which is the same as the previous observation on the x_2ox_3 plane (Fig. 4(d)). This simulation result is in agreement with previous work [25], which has shown that it is impossible to have APBs in a two-phase mixture of ordered and disordered phases if the specific interfacial energy of APB is two times higher than that of interface, which is usually the case. The above result is based on one particular plane. But the tendency in other planes is quite similar. For example, on the external x_1ox_2 plane ($x_3 = 128$) of the 3D unit cell, one can

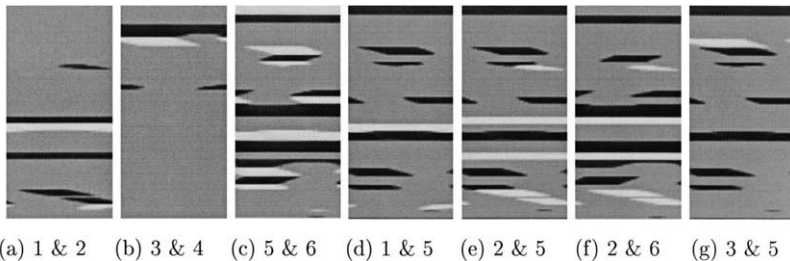


Fig. 5. Variants in contact on the x_2ox_3 surface plane of the 3D unit cell at $\tau = 100$. The first variant is in white and the second in black.

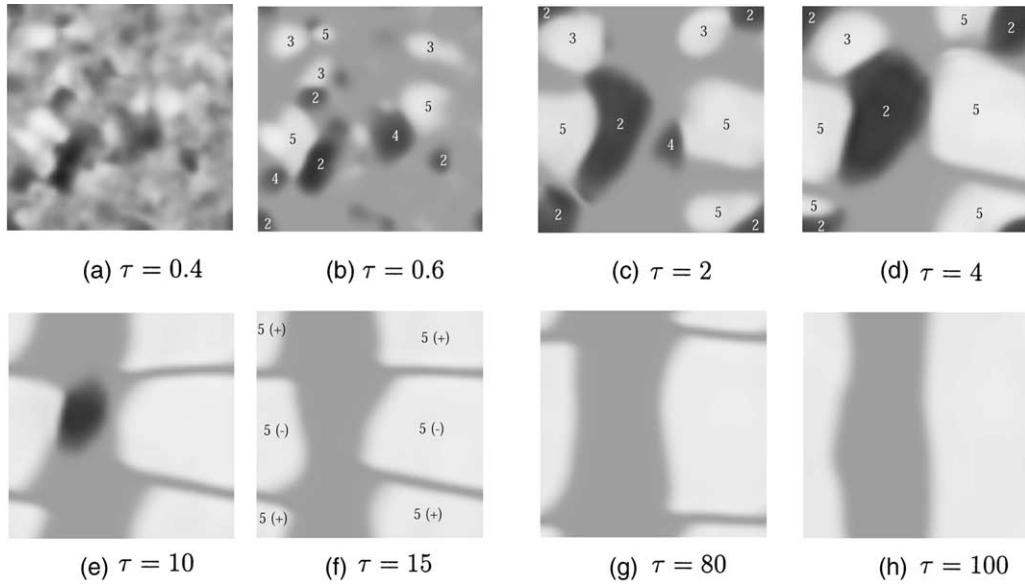


Fig. 6. Morphological evolution on one $x_1o x_2$ plane of the 3D unit cell with $x_3 = 50$. The shades of gray correspond to the relative value of $(\eta_1^2 - \eta_2^2) + (\eta_3^2 - \eta_4^2) + (\eta_5^2 - \eta_6^2)$ and the numbers in the figure represent variant number.

also find that there is a decrease in variant number at earlier stage and eventually the whole plane is occupied by a single variant.

It should be noted that the interfaces between bordering variants, for example, those in Fig. 6(c) between variants 2 and 5, 2 and 3, 4 and 5, do not have strong preference for certain crystallographic planes, which is in agreement with experimental observations [7]. In our previous study of congruent transformation from hexagonal to orthorhombic [18, 19], on the $(0001)_{o2}$ plane, the interfaces separating twin-related variants are always the invariant $\{110\}$ or $\{130\}$ planes. Although on the $(0001)_{o2}$ plane, the relative misfit among orientation variants of γ TiAl due to the ordering along three $\langle 002 \rangle_\gamma$ directions [equation (2)] is almost identical (different only by the shear magnitude) to that among six orientation variants of the O-phase (see equation (14) in [19]), the c -axis normal to the $(0001)_{o2}$ plane is not an invariant line any more in the present case due to the shear deformation of every two atomic layers for the $hcp \rightarrow fcc$ transformation, and thus it is impossible to form invariant planes between two bordering variants. As a result, there is no oriented interface between bordering variants on $(0001)_{o2}$.

3.5. Effect of interfacial energy anisotropy

In this study both interfacial energy anisotropy and elastic energy accommodation are considered. To investigate separately the effect introduced by the interfacial energy anisotropy, a simulation has been performed in which the only difference from the foregoing simulation is that the elastic energy term is not taken into account in the total free energy formulation, which is realized by simply setting $\phi = 0$

instead of 15. Corresponding microstructure evolution on the $x_2o x_3$ surface plane of the 3D unit cell is shown in Fig. 7, where the color scheme is the same as employed in Fig. 6.

As can be seen from Fig. 7, the microstructure features are very different from what have been observed in the previous case. First, the volume fraction of the γ phase is higher than $\sim 95\%$ which is expected from the mean composition of the alloy and the local specific free energy curve presented in Fig. 2, while in

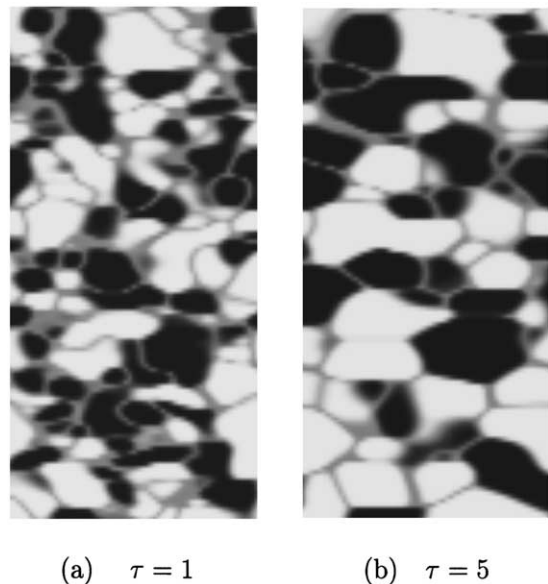


Fig. 7. Morphological evolution on the $x_2o x_3$ surface plane of the 3D unit cell without the influence of elastic energy. The shades of gray are the same as those employed in Fig. 6.

the previous case the volume fraction of the γ TiAl is $\sim 70\%$ (Fig. 3(f) or 4(i)), which demonstrates a strong effect of the elastic interaction on the phase equilibrium [26, 27]. Second, no lamellar structure at all is formed, which indicates that the elastic interaction plays a key role in the formation of the lamellar structure. Third, the kinetic process without elastic interaction is fast. The simulation is stopped after a relatively short-time coarsening because the coarsening in this case is much faster as compared to the previous simulation where elastic interaction leads to the formation of lamellae of planar interfaces. The microstructure is characterized by some ellipsoid-like variants, which is similar to that of an ordinary grain growth driven by reduction of grain boundary energy. The ellipsoid-like morphology is caused by the anisotropy in interfacial energy. In the simulations by far, we have assumed a smaller specific interfacial energy along the x_3 direction, namely $[0001]_{\alpha_2}$. If we ignore this anisotropy by setting $\beta_{11} = \beta_{22} = \beta_{33} = 3.0$ (we assumed $\beta_{11} = \beta_{22} = 5\beta_{33} = 3.0$ in the foregoing simulations) and repeat the simulation as presented in Fig. 7, one can find that the ellipsoid-like morphology does not exist any more (Fig. 8). Instead, the dominant morphology of the various variants is like a sphere, which is a result of minimizing the isotropic interfacial energy.

3.6. Limitations of the model

In this work, we assumed a homogeneous nucleation process and heterogeneous nucleation of γ on stacking faults is ignored. Corresponding study on the effect of heterogeneous nucleation is underway. In our formulation, the transformation mode is predetermined by the selection of the structural order para-

meters which may exclude some possible transformation modes occurring at intermediate stages of the transformation. For example, the deformation modes in the SFTS, namely the ordering phase separation on the $(0001)_{\alpha_2}$ and the shear deformation, which transforms *hcp* to *fcc*, are assumed to occur simultaneously.

While most important input data are based on experimental work, for example, the elastic constants, lattice parameters for both phases, and crystallographic orientation relationship, etc., the local specific free energy is not based on experimental data. As has been mentioned earlier, the local specific free energy mainly provides driving force for the $\alpha_2' \rightarrow \gamma$ transformation. So its specific form is not critical as far as the morphological pattern is concerned. However, for the purpose of alloy design, we will need a more comprehensive model, in which the temperature effect on the local specific free energy has to be taken into account. Development of such a model to use some thermodynamic database for the construction of our local specific free energy model is under way.

4. SUMMARY

A 3D phase-field model is developed to simulate the formation of lamellar structure in γ TiAl system. All the essential driving forces for the phase transformation, including the bulk chemical free energy, interfacial energy and elastic energy, are considered in the model. Without any prior assumption as how the microstructure may develop, some essential features of the lamellar structure have been predicted. It is found that the formation and dynamic evolution of the lamellar structure are dominated by accommodation of the coherency elastic strain arising from the lattice misfit between the low-symmetry product phase $\gamma(L1_0)$ and the high-symmetry phase α_2 (DO_{19}), as well as among the various orientation variants of the product phase. Also the relatively higher population of twin-related domains over pseudo-twin-related domains is related to the strain-induced correlated nucleation and elastic energy minimization.

Acknowledgements—The author thanks Drs H. L. Fraser, S. A. Dregia, A. Khachatryan and B. Viswanathan for helpful discussions. We acknowledge financial support from the OSU postdoc fellowship (Wen), NSF DMR-9703044 (Wang and Wen), and DMR-96-33719 (Chen). Hazzledine acknowledges support from the AFRL materials and Manufacturing Directorate contract #F 33615-96-C-5258 with UES Inc. The simulation was performed at the San Diego Supercomputer Center.

REFERENCES

- Kim, Y. -W. and Dimiduk, D. M., *JOM*, 1991, **August**, 40.
- Sastry, S. M. L. and Lipsitt, H. A., in *Titanium'80*, ed. H. Kimura and O. Izumi. Metallurgical Society of AMIE, Warrendale, PA, 1980, p. 1231.
- Yamaguchi, M., Nishitani, S. R. and Shirai, Y., in *High-Temperature Aluminides and Intermetallics*, ed. S.H.

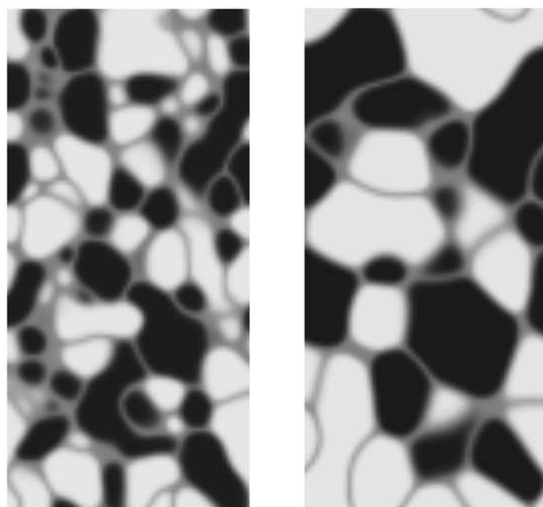


Fig. 8. Morphological evolution on the x_2x_3 surface plane of the 3D unit cell without the influence of elastic energy and anisotropy of the interfacial energy coefficients. The shades of gray are the same as those employed in Fig. 6.

- Wang, C.T. Liu, D.P. Pope and J.O. Stiegler. Metals and Materials Society, Warrendale, PA, 1990, p. 63.
4. Kim, Y. -W., in *High-Temperature Oriented Intermetallic Alloys IV*, vol. 213, ed. L.A. Johnson, D.P. Pope and J.O. Stiegler. Materials Research Society, Pittsburgh, PA, 1991, p. 777.
 5. Hall, E. L. and Huang, S. C., *J. Mater. Res.*, 1989, **4**, 595.
 6. Blackburn, M. J., in *Technology and Application of Titanium*, ed. R. T. Yaffee and N. E. Promisel. Pergamon, Oxford, 1970, p. 633.
 7. Inui, H., Oh, M. H., Nakamura, A. and Yamaguchi, M., *Phil. Mag. A*, 1992, **66**, 539.
 8. Huang, S. C. and Shih, D. S., in *Proceedings of the Symposium on Microstructure/Property Relationship in Titanium Aluminides and Alloys*, ed. Y. W. Kim and R. P. Boyer. Minerals Metals and Materials Society, Warrendale, PA, 1990, p. 105.
 9. Kim, Y. W., *Acta metall.*, 1992, **40**, 1121.
 10. Khachaturyan, A. G., *Theory of Structural Transformations in Solids*. Wiley, New York, 1983.
 11. Johnson, W. C., Influence of elastic stress on phase transformations, in *Lectures on the Theory of Phase Transformations*, ed. H. I. Aaronson. TMS-AIME, New York, 1999.
 12. Wang, Y. and Chen, L. Q., *Methods in Materials Research*. Unit 2a.3., Wiley, New York, 2000.
 13. Chen, L. Q. and Wang, Y., *JOM*, 1996, **48**, 13.
 14. Denquin, A. and Naka, A., *Acta metall.*, 1996, **44**, 343.
 15. Grinfeld, M. A., Hazzledine, P. M., Shoykhet, B. and Dimiduk, D. M., *Meta. Mater. Trans. A*, 1998, **29A**, 937.
 16. Landau, L. D. and Lifshitz, E. M., *Course of Theoretical Physics, Theory of Elasticity*, 3rd ed., vol. 7, Pergamon Press, Oxford, 1986
 17. Lifshitz, E. M. and Pitaevskii, L. P., *Statistical Physics*. Pergamon Press, Oxford, 1980.
 18. Wen, Y. H., Wang, Y. and Chen, L. Q., *Philos. Mag. A*, 2000, **80**, 1967.
 19. Wen, Y. H., Wang, Y. and Chen, L. Q., *Acta mater.*, 1999, **47**, 4375.
 20. Wen, Y. H., Wang, Y., Bendersky, L. A. and Chen, L. Q., *Acta mater.*, 2000, **48**, 4125.
 21. Tanaka, K., Okamoto, K., Inui, H., Minonishi, Y., Yamaguchi, M. and Koiwa, M., *Phil. Mag. A*, 1996, **73**, 1475.
 22. Wang, Y. and Khachaturyan, A. G., *Acta mater.*, 1997, **45**, 759.
 23. Yang, J. H. and Wayman, C. M., *Materials Characterization*, 1992, **28**, 23.
 24. Yang, J. H. and Wayman, C. M., *Materials Characterization*, 1992, **28**, 37.
 25. Wang, Y., Banerjee, D., Su, C. C. and Khachaturyan, A. G., *Acta metall.*, 1998, **46**, 2983.
 26. Larché, F. C. and Cahn, J. W., *Acta metall.*, 1985, **33**, 331.
 27. Wen, Y. H., Wang, Y. and Chen, L. Q., *Acta mater.*, 2001, **49**, 13.